LETTER

https://doi.org/10.1038/s41586-019-1402-1

Visualizing electrostatic gating effects in two-dimensional heterostructures

Paul V. Nguyen[1], Natalie C. Teutsch[2], Nathan P. Wilson[1], Joshua Kahn[1], Xue Xia[2], Abigail J. Graham[2], Viktor Kandyba[3], Alessio Giampietri[3], Alexei Barinov[3], Gabriel C. Constantinescu[4], Nelson Yeung[2], Nicholas D. M. Hine[2], Xiaodong Xu[1,5]*, David H. Cobden[1]* & Neil R. Wilson[2]*

The ability to directly monitor the states of electrons in modern field-effect devices—for example, imaging local changes in the electrical potential, Fermi level and band structure as a gate voltage is applied—could transform our understanding of the physics and function of a device. Here we show that micrometre-scale, angle-resolved photoemission spectroscopy[1–3] (microARPES) applied to two-dimensional van der Waals heterostructures[4] affords this ability. In two-terminal graphene devices, we observe a shift of the Fermi level across the Dirac point, with no detectable change in the dispersion, as a gate voltage is applied. In two-dimensional semiconductor devices, we see the conduction-band edge appear as electrons accumulate, thereby firmly establishing the energy and momentum of the edge. In the case of monolayer tungsten diselenide, we observe that the bandgap is renormalized downwards by several hundreds of millielectronvolts—approaching the exciton energy—as the electrostatic doping increases. Both optical spectroscopy and microARPES can be carried out on a single device, allowing definitive studies of the relationship between gate-controlled electronic and optical properties. The technique provides a powerful way to study not only fundamental semiconductor physics, but also intriguing phenomena such as topological transitions[5] and many-body spectral reconstructions under electrical control.

In ARPES, one measures the distribution of the energy and momentum of electrons photoemitted from a solid sample that is being subjected to narrow-spectrum ultraviolet or X-ray excitation. This provides information about the energy and momentum of the initial occupied electron states, and hence the band structure and Fermi level. As electrons are emitted only from very near the sample surface, ARPES is not useful for studying conventional semiconductor devices. On the other hand, it is well suited to probing two-dimensional (2D) materials, and has been applied to films of graphene[6], transition metal dichalcogenides (MX_2, where M is molybdenum (Mo), tungsten (W), tantalum (Ta) or another transition metal, and X is sulfur (S), selenium (Se) or tellurium (Te))[7,8], and others[9,10]. Although the excitation spot size is typically measured in millimetres, efforts have been made in the past decade[2] to perform ARPES with a focused beam suitable for small or nonuniform samples. Micrometre-scale spot sizes (hence 'μ-ARPES') have been achieved in at least four commissioned synchrotron beamlines by using Schwarzschild objectives[1], Fresnel zone plates[2,3], or capillary mirror optics[11]. MicroARPES has allowed the study of atomically thin exfoliated flakes of 2D materials, which are typically tens of micrometres or fewer in size[12], and of heterostructures[4] made by stacking such flakes of different materials[13,14], revealing for example band offsets and interlayer hybridization[15–17]. Such 2D heterostructures can be made

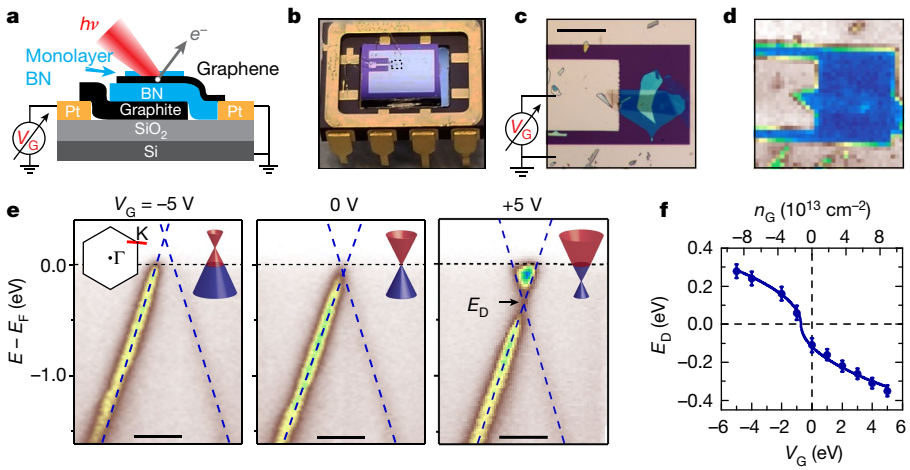

Fig. 1 | Visualizing electrostatic gating of monolayer graphene. **a**, Diagram of a 2D heterostructure device, which consists of a stack comprising graphene encapsulated by BN on a graphite back gate. A focused micrometre-size X-ray beam spot (energy $h\nu$) generates photoemitted electrons (e^-) (see Methods). The graphene is grounded while a gate voltage, V_G, is applied to the gate. **b**, Optical image of a device mounted in a standard dual in-line package. **c**, Magnified optical image of the dotted box in panel **b**, showing the stack. Scale bar, 50 μm. **d**, SPEM image of the same area. **e**, Energy-momentum slices near the graphene K-point (along the red line in the Brillouin zone shown in the inset at the left), at the labelled gate voltages. The blue dashed lines are linear dispersion fits; the Dirac-point energy E_D is deduced from their crossing point. Scale bars, 0.2 $Å^{-1}$. Inset are schematics of the graphene Dirac cone at each V_G, contrasting filled (purple) and empty (red) states. **f**, Gate dependence of E_D, with error bars obtained from the fitting procedure. The solid line is a fit based on the dispersion of graphene, with the gate-induced electron density (n_G) shown on the top axis and calculated from the capacitance (see Methods).

[1]Department of Physics, University of Washington, Seattle, WA, USA. [2]Department of Physics, University of Warwick, Coventry, UK. [3]Elettra-Sincrotrone Trieste SCpA, Basovizza, Italy. [4]Theory of Condensed Matter Group, Cavendish Laboratory, University of Cambridge, Cambridge, UK. [5]Department of Materials Science and Engineering, University of Washington, Seattle, WA, USA.
*e-mail: xuxd@uw.edu; cobden@uw.edu; neil.wilson@warwick.ac.uk

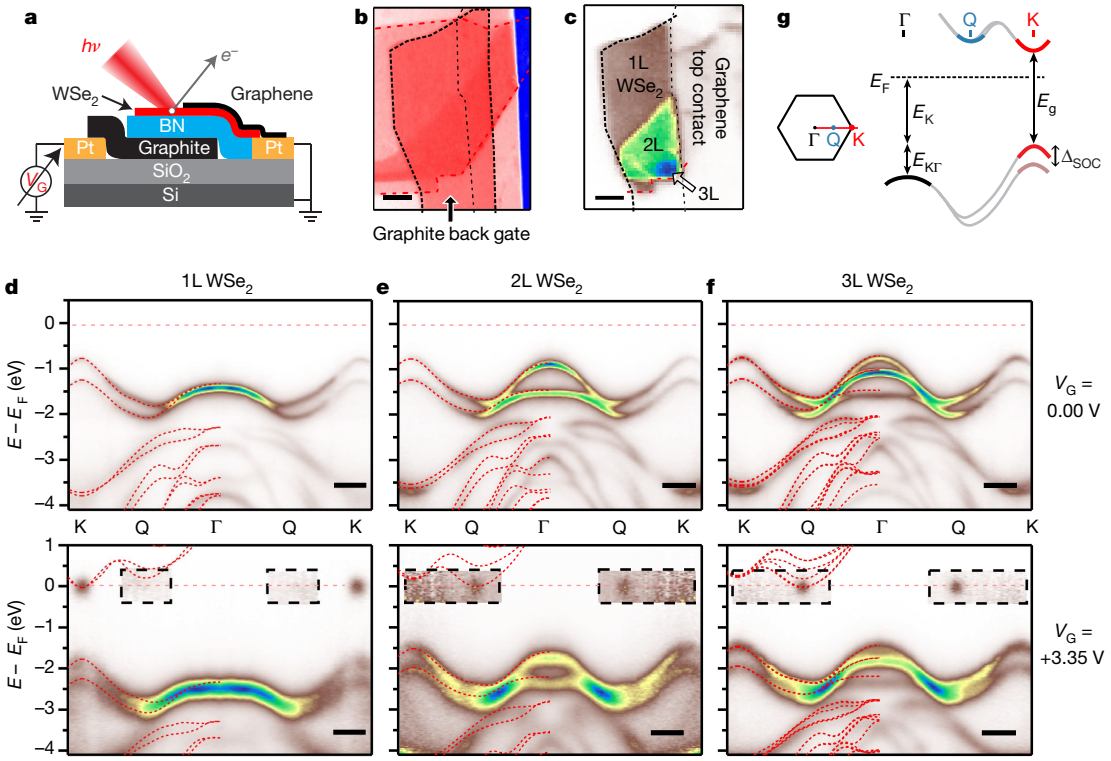

Fig. 2 | Layer-number-dependent CBE in WSe_2. a, Diagram of a device incorporating a WSe_2 flake, with an overlapping ground graphene top contact and gate voltage applied to the graphite back gate. **b**, **c**, Optical (**b**) and SPEM (**c**) images of WSe_2 device 1 (BN thickness (d_{BN}) = 7.4 ± 0.5 nm), with monolayer (1L), bilayer (2L) and trilayer (3L) regions identified. Scale bars, 5 μm. **d**–**f**, Energy-momentum slices along Γ–K for 1L, 2L and 3L regions respectively. The upper panels are at $V_G = 0$ and the lower ones at $V_G = +3.35$ V. The intensity in the dashed boxes is multiplied by 20. The fuzzy spots signal population of the CBE. Scale bars, 0.3 $Å^{-1}$. The data have been reflected about Γ to aid comparison with electronic structure calculations (GW approximation; red dashed lines). **g**, Brillouin zone of MX_2 (left) and diagram of the bands along Γ–K (right), showing definitions of the energy parameters discussed in the text.

into electrical and optical devices[18] by incorporating metal electrodes, opening up the possibility of using microARPES to monitor electronic structure in operating devices.

A major limitation of ARPES is that it probes only occupied electron states. A semiconductor sample must therefore be electron-doped in order to obtain a signal from the conduction band. Doping is usually achieved by depositing electropositive atoms such as alkali metals[6–8,13] on the surface. This process cannot be controlled accurately and can only be reversed by high-temperature annealing; moreover, it chemically perturbs the electronic structure and introduces disorder through the random distribution of dopants. Here we demonstrate purely electrostatic doping, which has none of these disadvantages. We thereby obtain momentum-resolved electronic spectra and direct visualization of Fermi-level shifts and band-structure changes induced by applying a gate voltage.

We first demonstrate and validate the technique using graphene, then go on to apply it to the 2D MX_2 semiconductors, which are of interest for valleytronics and other applications[18,19]. Although it is widely believed that all monolayer MX_2 semiconductors have a direct bandgap at the corner (point K) of the hexagonal Brillouin zone, the location of the conduction-band edge (CBE) is not known with certainty. This is illustrated by the wide range of reported bandgap values for monolayer WSe_2, from 1.4 eV to 2.2 eV (refs [8,20–24]). Also unclear is when the local conduction-band minimum at the lower-symmetry point Q comes into play[21,25]. Using electrostatic doping in microARPES, we confirm that the CBE is at K in all of the monolayer semiconductors—MoS_2, $MoSe_2$, WS_2 and WSe_2—and in each case we obtain a measure of the bandgap. We also study the layer-number dependence in WSe_2, finding that the CBE moves to Q in the bilayer, and measure for the first time the renormalization of the band structure on gating.

In our graphene devices, a graphene sheet is capped by monolayer hexagonal boron nitride (BN), supported on a BN flake over a graphite gate (Fig. 1a), and located in a gap between two platinum electrodes on an SiO_2/Si substrate chip (Fig. 1b, c; see Methods and Extended Data Fig. 1). A similar structure with two contacts to the graphene would

Table 1 | Measured band-structure parameters of MX_2 semiconductors

	Δ_{SOC} (eV)	E_K ($V_G = 0$) (eV)	$E_{K\Gamma}$ ($V_G = 0$) (eV)	m_K^*/m_e	E_g (eV)
1L MoS_2	0.17 ± 0.04	1.93 ± 0.02	0.14 ± 0.04	0.7 ± 0.1	2.07 ± 0.05
1L $MoSe_2$	0.22 ± 0.03	1.04 ± 0.02	0.48 ± 0.03	0.5 ± 0.1	1.64 ± 0.05
1L WS_2	0.45 ± 0.03	1.43 ± 0.02	0.39 ± 0.02	0.5 ± 0.1	2.03 ± 0.05
1L WSe_2	0.485 ± 0.010	0.80 ± 0.01	0.62 ± 0.01	0.42 ± 0.05	1.79 ± 0.03
2L WSe_2	0.501 ± 0.010	0.75 ± 0.01	0.14 ± 0.01	0.41 ± 0.05	1.51 ± 0.03 *
3L WSe_2	0.504 ± 0.010	0.74 ± 0.01	0.00 ± 0.01	0.40 ± 0.05	1.46 ± 0.03 *

As defined in Fig. 2g, Δ_{SOC} is the spin–orbit splitting of the valence band at K; E_K is the valence-band edge at $V_G = 0$; $E_{K\Gamma} = E_K - E_\Gamma$ is the difference between the valence-band edges at K and Γ at $V_G = 0$; m_K^* is the effective mass of the valence-band edge at K in units of the free electron mass m_e; and E_g is the bandgap measured at gate-induced electron density $n_G = 1.0 \pm 0.2 \times 10^{12}$ cm^{-2}. The stage temperature was 100 K for WSe_2 and 105 K for the others.
*Indirect measurement, with CBE at Q.

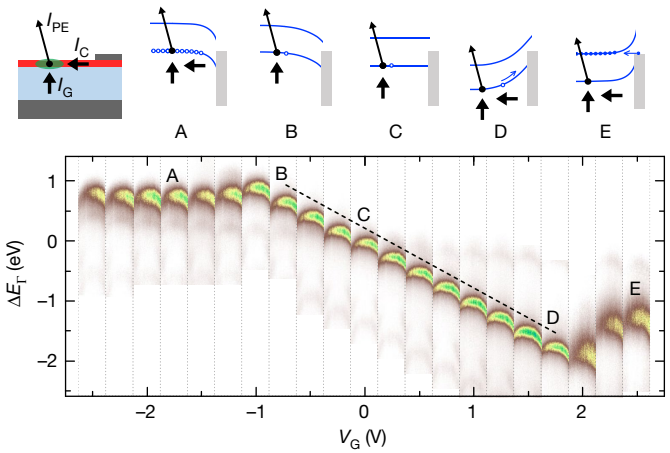

Fig. 3 | Electrostatic gating of monolayer WSe_2. Each vertical strip in the chart at the bottom is an energy-momentum slice, 0.6 $Å^{-1}$ wide, through Γ in WSe_2 device 2 ($d_{BN} = 6.0 \pm 0.5$ nm), measured at the gate voltages shown on the *x* axis. ΔE_Γ is the photoelectron kinetic energy measured relative to the Γ maximum at $V_G = 0$. The dashed line has slope $-1/e$. Above left is a device schematic, indicating the photoemission current I_{PE} from the beam spot, current I_C from the graphene contact, and current I_G from the gate due to photoconductivity of the BN. The schematic band diagrams on the right indicate the situations at the gate voltages labelled A to E. The grey rectangle is the graphene Fermi sea; the blue lines are the WSe_2 conduction- and valence-band edges; the blue circles represent gate-induced electrons (solid) and holes (empty); the black arrows correspond to the arrows in the left-hand diagram and indicate when I_G and I_C must be taken into account. Blue arrows indicate contact current carried by electrons or holes.

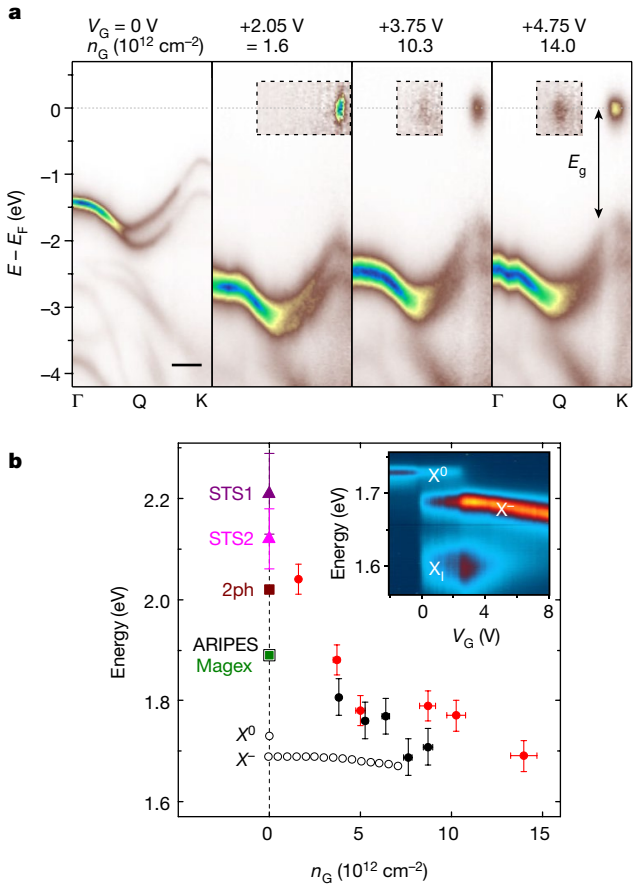

Fig. 4 | Renormalization of the bandgap and comparison with optical spectroscopy. a, Energy-momentum slices along Γ–K for monolayer WSe_2 in device 1 at a series of V_G, with doping n_G also shown. Scale bar, 0.3 $Å^{-1}$. The intensity in the dashed box is multiplied by 20 at +2.05 V and by 40 at higher values of V_G. The definition of the bandgap, E_g, is indicated. **b**, Dependence of the bandgap on n_G for device 1 (red circles) and also device 3 ($d_{BN} = 4.5 \pm 0.5$ nm; solid black circles) at 100 K. Energy error bars are from best fits to the spectra; density error bars are from uncertainty in the BN thickness. Also plotted (black open circles) are the photoluminescence peak positions for the neutral exciton (X^0) and negative trion (X^-) in device 3 at the same temperature. The inset shows the photoluminescence data, with an impurity-bound exciton peak, X_I, also labelled. The points plotted at $n_G = 0$ are measurements of the bandgap from other techniques taken from the literature: STS1 (ref. [20]; purple triangle) and STS2 (ref. [21]; pink triangle) are from scanning tunnelling spectroscopy measurements of graphite at temperatures of 4.5 K and 77 K respectively; 2ph (brown square) is from two-photon absorption[22] on SiO_2 at 300 K; ARIPES (black open square) is from inverse photoemission[23] on sapphire at 300 K; and Magex (green solid square) is from magneto-optical measurements[24], encapsulated in BN at 4 K.

function as a high-mobility transistor[26]. We used scanning photoemission microscopy (SPEM) to locate the sample in the ARPES chamber (Fig. 1d; see Methods). Figure 1e shows energy, $E - E_F$ (where E is the measured photoelectron kinetic energy and E_F is the kinetic energy of electrons removed from the Fermi level) versus in-plane momentum for a slice through the Dirac cone near the graphene zone corner K, acquired at a series of gate voltages (V_G) at 105 K. As expected, the Dirac-point energy, E_D, shifts from above E_F at $V_G = -5$ V to below E_F at +5 V. Fitting a linear dispersion, $E(k) = E_D \pm \hbar v_F k$ (blue dashed lines in Fig. 1e; $\hbar$ is Planck's constant and k is the in-plane momentum), gives E_D and the Fermi velocity, v_F. The variation of E_D with V_G (Fig. 1f) is consistent with the expected form for this dispersion (solid line; see Methods). No modification of the dispersion near E_D, as could arise because of interactions, is detectable with the present spectral resolution (see Extended Data Fig. 2). We find that $v_F = (9.3 \pm 0.1) \times 10^5$ ms^{-1} at $V_G = 0$, with a weak V_G dependence (see Extended Data Fig. 3).

The consistency of the above properties with the literature on graphene, together with the observation that the spectrum is undistorted as V_G is changed, implies that the photoelectron trajectories are not affected by stray electric fields resulting from the gate voltage or charging effects. We conclude that our technique produces accurate local electronic spectra during live electrostatic gating.

To study gate doping of 2D semiconductors, we incorporate an MX_2 flake into the stack on top of the BN and partially overlapped by graphene, which acts as a contact to the MX_2 (Fig. 2a). Figure 2b, c shows optical and SPEM images of a device with a WSe_2 flake that has monolayer (1L), bilayer (2L) and trilayer (3L) regions. Figure 2d–f shows momentum slices obtained with the beam spot on each of these regions and along Γ–K in the WSe_2 Brillouin zone at a temperature of 100 K (Fig. 2g, inset). As expected, at $V_G = 0$ (upper row) only the valence bands can be seen. Their evolution with layer number is consistent with the literature[27] and matches well with the overlaid theoretical predictions (the GW approximation; see Methods). At $V_G = +3.35$ V (lower row), an additional spot appears near E_F. The size of this conduction-band feature is determined solely by the resolution of the measurement. In 1L WSe_2 the spot is located at K, whereas in 2L and 3L it is at Q (Fig. 2g and Extended Data Fig. 4). This is consistent with evidence from photoluminescence[25] that the gap is direct at K in the monolayer, but indirect for two or more layers.

Table 1 displays the band parameters for 1L–3L WSe_2, as well as for other monolayer MX_2 species, derived[15] from measurements on this and other devices (Extended Data Fig. 5). We determined the bandgap, $E_g = E_C - E_K$, where E_C is the energy of the CBE, at a gate doping level of n_G approximately equal to 10^{13} cm^{-2}, for which $E_F - E_C$ is approximately 30 meV (see Methods). We also list the simultaneously determined hole effective mass m_K^*, the valence-band edge E_K, the spin–orbit splitting Δ_{SOC}, and $E_{K\Gamma}$ (the latter three being defined in Fig. 2g)—all measured for the first time on a hexagonal BN substrate with no cap and with greater precision than in previous reports.

We now consider the full gate dependence of microARPES spectra. Figure 3 shows the behaviour of the top of the valence band at Γ, where the photoemission signal is strongest, for our monolayer WSe_2 device 2.

At low V_G (range labelled B–C–D in Fig. 3), the spectrum shifts nearly linearly with a slope of $-1/e$, where e is the electron charge, implying that the electrostatic potential in the WSe_2 tracks the gate potential when it is undoped. For V_G values of more than +2.1 V (labelled E in Fig. 3) or less than −1.5 V (labelled A), the spectrum becomes almost independent of V_G, implying that these are the thresholds for electron and hole accumulation, respectively. The behaviour can be understood in more detail with reference to the corresponding band diagrams shown above in Fig. 3, taking into account the balance of the current of photoemitted electrons, I_{PE}, and the currents into the beam spot from the contact, I_C, and the gate, I_G, as indicated in the sketch at the top left (see Methods).

Note that no change in spectral widths is seen as long as the WSe_2 is insulating (range B–D in Fig. 3), but above threshold (range D–E) all features are smeared in energy by a similar amount. This can be explained by inhomogeneous broadening due to variation of the potential across the beam spot, associated with lateral current flow in the WSe_2. Refinement of the technique to reduce this effect may allow studies of changes in intrinsic broadening with doping.

Figure 4a shows spectra from monolayer WSe_2 device 1 at $V_G = 0$ (for reference) and at selected gate voltages well above threshold (about +1.5 V). In this regime we derive the gate doping, n_G, also shown, from the gate capacitance and threshold voltage (see Methods). The CBE becomes visible at K for n_G values of more than about 10^{12} cm^{-2}, and at Q for values of more than roughly 10^{13} cm^{-2}, when E_K is roughly 30 meV below E_F. We conclude that the conduction-band minimum at Q is higher than that at K. Scanning tunnelling spectroscopy[21] also indicates that for 1L WSe_2 these minima are very close. The form of the valence bands does not change discernibly with increasing n_G, but they shift upwards in energy while the CBE is pinned at E_F, implying that the bandgap decreases.

Optical spectroscopy can be performed on the same devices, and under the same conditions, as the microARPES measurements, eliminating uncertainties due to differences in sample quality, dielectric environment, gate voltage and temperature[28–30]. Figure 4b shows both the microARPES determination of E_g (black solid circles) and the photoluminescence peak positions (black empty circles), E_{X^0} and E_{X^-}, for neutral (X^0) and charged (X^-) excitons, for monolayer WSe_2 device 3 as a function of gate doping at 100 K. Also shown are the values of E_g from device 1 (red solid circles), which agree to within the uncertainty. It is apparent that E_g decreases systematically, by around 400 meV overall as n_G rises to 1.5×10^{13} cm^{-2}. Such renormalization of the bandgap with static doping is expected to occur in a semiconductor as a result of free-carrier screening[31], though it has not previously been so accessible to experiments.

Also plotted in Fig. 4b are values of the bandgap at $n_G = 0$ inferred from several other techniques. An extrapolation of E_g measured by microARPES to $n_G = 0$ is consistent with scanning tunnelling spectroscopy (STS) measurements, which put it in the range 2.1–2.2 eV. Comparison with E_{X^0} supports arguments that the binding energy of neutral excitons in this material is very large[28], at several hundred millielectronvolts. E_g decreases much more quickly than E_{X^-} with doping, implying dramatic weakening of the exciton binding—another expected effect of free-carrier screening[29]. Finally, the smaller values of E_g reported in monolayers doped with alkali metals (down to 1.4 eV for 1L WSe_2) are consistent with an extrapolation of the renormalization process to higher n_G values[7,8].

The ability to measure changes in the electronic bands in 2D field-effect devices opens up many interesting possibilities. For example, it could be used to study electric-field tuning of the bands across topological phase transitions[5]; to investigate the doping dependence of spectra in correlated electron systems such as in superconductors, Mott insulators, and charge-density-wave materials; to observe spectral reconstructions in structures with moiré superlattice modulations[32]; and, with the addition of circularly polarized light or a spin-resolved spectrometer, to study electrically controlled magnetic phenomena[33].

Online content

Any methods, additional references, Nature Research reporting summaries, source data, extended data, supplementary information, acknowledgements, peer review information; details of author contributions and competing interests; and statements of data and code availability are available at https://doi.org/10.1038/s41586-019-1402-1.

Received: 2 October 2018; Accepted: 7 May 2019;
Published online 17 July 2019.

1. Dudin, P. et al. Angle-resolved photoemission spectroscopy and imaging with a submicrometre probe at the Spectromicroscopy-3.2L beamline of Elettra. *J. Synchrotron Radiat.* **17**, 445–450 (2010).
2. Rotenberg, E. & Bostwick, A. MicroARPES and nanoARPES at diffraction-limited light sources: opportunities and performance gains. *J. Synchrotron Radiat.* **21**, 1048–1056 (2014).
3. Iwasawa, H. et al. Buried double CuO chains in $YBa_2Cu_4O_8$ uncovered by nano-ARPES. *J. Phys. Condens. Matter* **4**, 9015–9022 (2019).
4. Novoselov, K. S., Mishchenko, A., Carvalho, A. & Castro Neto, A. H. 2D materials and van der Waals heterostructures. *Science* **353**, aac9439 (2016).
5. Tong, Q. et al. Topological mosaics in moiré superlattices of van der Waals heterobilayers. *Nat. Phys.* **13**, 356–362 (2017).
6. Bostwick, A., Ohta, T., Seyller, T., Horn, K. & Rotenberg, E. Quasiparticle dynamics in graphene. *Nat. Phys.* **3**, 36–40 (2007).
7. Riley, J. M. et al. Negative electronic compressibility and tunable spin splitting in WSe_2. *Nat. Nanotechnol.* **10**, 1043–1047 (2015).
8. Zhang, Y. et al. Electronic structure, surface doping, and optical response in epitaxial WSe_2 thin films. *Nano Lett.* **16**, 2485–2491 (2016).
9. Kim, J. et al. Observation of tunable band gap and anisotropic Dirac semimetal state in black phosphorus. *Science* **349**, 723–726 (2015).
10. Tang, S. et al. Quantum spin Hall state in monolayer 1T′-WTe_2. *Nat. Phys.* **13**, 683–687 (2017).
11. Koch, R. J. et al. Nano focusing of soft X-rays by a new capillary mirror optic. *Synchrotron Radiat. News* **31**, 50–52 (2018).
12. Zhang, H. et al. Resolving deep quantum-well states in atomically thin 2H-$MoTe_2$ flakes by nanospot angle-resolved photoemission spectroscopy. *Nano Lett.* **18**, 4664–4668 (2018).
13. Katoch, J. et al. Giant spin-splitting and gap renormalization driven by trions in single-layer WS_2/h-BN heterostructures. *Nat. Phys.* **14**, 355–359 (2018).
14. Cucchi, I. et al. Microfocus laser-angle-resolved photoemission on encapsulated mono-, bi-, and few-layer 1T′-WTe_2. *Nano Lett.* **19**, 554–560 (2019).
15. Wilson, N. R. et al. Determination of band offsets, hybridization, and exciton binding in 2D semiconductor heterostructures. *Sci. Adv.* **3**, e1601832 (2017).
16. Jin, W. et al. Tuning the electronic structure of monolayer graphene/MoS_2 van der Waals heterostructures via interlayer twist. *Phys. Rev. B* **92**, 201409 (2015).
17. Pierucci, D. et al. Band alignment and minigaps in monolayer MoS_2-graphene van der Waals heterostructures. *Nano Lett.* **16**, 4054–4061 (2016).
18. Liu, Y. et al. Van der Waals heterostructures and devices. *Nat. Rev. Mater.* **1**, 16042 (2016).
19. Schaibley, J. R. et al. Valleytronics in 2D materials. *Nat. Rev. Mater.* **1**, 16055 (2016).
20. Yankowitz, M., McKenzie, D. & LeRoy, B. J. Local spectroscopic characterization of spin and layer polarization in WSe_2. *Phys. Rev. Lett.* **115**, 136803 (2015).
21. Zhang, C. et al. Probing critical point energies of transition metal dichalcogenides: surprising indirect gap of single layer WSe_2. *Nano Lett.* **15**, 6494–6500 (2015).
22. He, K. et al. Tightly bound excitons in monolayer WSe_2. *Phys. Rev. Lett.* **113**, 026803 (2014).
23. Park, S. et al. Direct determination of monolayer MoS_2 and WSe_2 exciton binding energies on insulating and metallic substrates. *2D Mater.* **5**, 025003 (2018).
24. Stier, A. V. et al. Magnetooptics of exciton Rydberg states in a monolayer semiconductor. *Phys. Rev. Lett.* **120**, 057405 (2018).
25. Zhao, W., Ribeiro, R. M. & Eda, G. Electronic structure and optical signatures of semiconducting transition metal dichalcogenide nanosheets. *Acc. Chem. Res.* **48**, 91–99 (2015).
26. Mayorov, A. S. et al. Micrometer-scale ballistic transport in encapsulated graphene at room temperature. *Nano Lett.* **11**, 2396–2399 (2011).
27. Liu, G., Xiao, D., Yao, Y., Xu, X. & Yao, W. Electronic structures and theoretical modelling of two-dimensional group-VIB transition metal dichalcogenides. *Chem. Soc. Rev.* **44**, 2643–2663 (2015).
28. Ugeda, M. M. et al. Giant bandgap renormalization and excitonic effects in a monolayer transition metal dichalcogenide semiconductor. *Nat. Mater.* **13**, 1091–1095 (2014).
29. Gao, S., Liang, Y., Spataru, C. D. & Yang, L. Dynamical excitonic effects in doped two-dimensional semiconductors. *Nano Lett.* **16**, 5568–5573 (2016).
30. Raja, A. et al. Coulomb engineering of the bandgap and excitons in two-dimensional materials. *Nat. Commun.* **8**, 15251 (2017).
31. Gao, S. & Yang, L. Renormalization of the quasiparticle band gap in doped two-dimensional materials from many-body calculations. *Phys. Rev. B* **96**, 155410 (2017).
32. Cao, Y. et al. Magic-angle graphene superlattices: a new platform for unconventional superconductivity. *Nature* **556**, 43–50 (2018).
33. Wang, H., Fan, F., Zhu, S. & Wu, H. Doping enhanced ferromagnetism and induced half-metallicity in CrI_3 monolayer. *EPL* **114**, 47001 (2016).

Publisher's note: Springer Nature remains neutral with regard to jurisdictional claims in published maps and institutional affiliations.

© The Author(s), under exclusive licence to Springer Nature Limited 2019

METHODS

Sample fabrication. Standard exfoliation and polycarbonate-film-based dry transfer[34] techniques were used. The smaller electrode contacts the graphite gate, as indicated in the optical micrograph in Fig. 1c (see also Extended Data Fig. 1). The larger electrode, which contacts the graphene, is grounded and covers most of the chip to minimize electrostatic distortion of the photoelectron spectrum when applying a gate voltage. The sample substrates are mounted in dual-inline packages using ultrahigh-vacuum, high-temperature-compatible silver epoxy and gold-wire-bonding. Bare wire is wrapped around the package pins, fixed using the epoxy, and used to make contact to leads on the ARPES sample mount.

Angle-resolved photoemission. Measurements were made at the Spectromicroscopy beamline of the Elettra light source[1]. Linearly polarized light, at 45° to the sample, was focused to a roughly 0.6-μm-diameter spot by a Schwarzschild objective. The photon energy was 27 eV except for the data in Fig. 1, where it was 74 eV. The hemispherical analyser with two-dimensional detector on a two-axis goniometer permitted a resolution of approximately 50 meV and 0.03 $Å^{-1}$. After mounting in the chamber on a scanning stage with 100-nm closed-loop positioning accuracy, the sample was located by SPEM. With the light focus fixed, the photoelectron intensity on the detector was acquired point by point as the sample was stepped relative to the light spot. In the SPEM images the colour corresponds to the integrated photoelectron intensity around Γ (over the full detector range of approximately 15°, corresponding to roughly 0.6 $Å^{-1}$ at 20 eV and 1.1 $Å^{-1}$ at 70 eV, and a binding-energy range of 0–2.5 eV in Fig. 1d and 0–3.5 eV in Fig. 2c and Extended Data Fig. 6) at that point on the sample. For spectral acquisition, the entrance slit to the analyser is in a fixed orientation, but its angular coordinates relative to the sample normal are controlled by the two-axis goniometer. For energy-momentum slices along Γ–K, as in Figs. 2, 3, a sequence of 2D slices was acquired with the goniometer moving the centre of the analyser entrance slit along the line in reciprocal space from Γ to K, mapping out a small volume in E and in-plane momentum k from which the Γ–K slice was later extracted. Over the few hours required to acquire these data, the sample drift was typically less than 1 μm. Prior to measurement, samples were annealed in ultrahigh vacuum at 650 K for several hours. The stage temperature was about 100 K (Fig. 2–4) or about 105 K (Fig. 1 and MoS_2, WS_2 and $MoSe_2$). Following standard practice, we plot $E - E_F$, the negative of the electron-binding energy, determined by fitting the Fermi–Dirac distribution to the drop in photoemitted intensity across the photoemission threshold.

Considerations of gate dependence and device operation. The devices have a thin hexagonal BN dielectric separating the graphite back-gate electrode from the upper 2D material (2DM) layer, which is either graphene itself or overlaps a graphene contact that in turn overlaps a metal (ground) electrode. When the 2DM is conducting, this constitutes a parallel-plate capacitor with geometric areal capacitance $C_g = (\varepsilon_0 \times \varepsilon_{BN}) / d_{BN}$, where ε_0 is the relative permittivity of free space, $\varepsilon_{BN} = 4.0 \pm 0.2$ is the out-of-plane (c-direction) dielectric constant for BN, and d_{BN} is the BN thickness. During photoemission, the electrochemical potential at the emission spot will differ from ground, by an amount ΔV, associated with current flow both to the contact and to the gate which is at voltage V_G, thus reducing the effective gate voltage determining the local carrier density to $V_G - \Delta V$. ΔV will not exceed the product of the effective electrical resistance, R, between the spot and ground electrode and the maximum current, which is no more than about 2 nA.

Graphene devices. For graphene devices, the band dispersion is not affected by doping to within 10% accuracy (see Extended Data Figs. 2, 3). In this case we expect $n_G = C_g(V_G - \Delta V - \Delta\mu/e)$, where $\Delta\mu = \Delta(E_F - E_D)$ is the chemical potential change due to gate doping (note that C_g is only the geometric capacitance, and the total capacitance is nonlinear in V_G). For graphene, R is less than about 1 kΩ and thus ΔV is less than approximately 2 μV, which is negligible. $\Delta\mu$ can be found from the ARPES spectrum at each gate voltage to an accuracy of roughly 20 meV. In the measurements shown in Fig. 1, $\Delta\mu/e$ is at least ten times smaller than V_G, and thus simply taking n_G is approx. equal to C_gV_G, the quantity plotted on the top axis of Fig. 1f, is accurate to less than 10%. When k_BT (where k_B is the Boltzmann constant) is much less than E_D (valid here since $k_BT = 9$ meV), from the conical Dirac dispersion one expects[35] E_D^2 is approx. equal to $\pi\hbar^2v_F^2(n_0 + n_G)$, where n_G is approximately equal to CV_G is the gate-induced 2D electron density, C the areal capacitance, and n_0 the residual electron density at $V_G = 0$. The solid line in Fig. 1f is a fit to this model, with C and n_0 treated as fitting parameters. The value of n_0 obtained is $(1.8 \pm 0.1) \times 10^{12}$ cm^{-2}, implying a somewhat high residual doping that may be due to contamination. The value of C is $(2.2 \pm 0.2) \times 10^{-7}$ F cm^{-2}, consistent with the geometrical capacitance; $(\varepsilon_0\varepsilon_{BN}) / d_{BN} = (2.5 \pm 0.2) \times 10^{-7}$ F cm^{-2}, derived from the BN thickness; $d_{BN} = 14 \pm 1$ nm, measured by atomic force microscopy; and the dielectric constant, $\varepsilon_{BN} = 4.0$, is taken from the literature[36–38]. Note also that the intensity near E_D is weak because these $E - k$ slices do not pass exactly through K. The much lower intensity on one side of the cone results from destructive interference between the two carbon sublattices[39].

MX_2 semiconductor devices. For MX_2 semiconductor devices, the situation is more complicated. At small V_G values, the doping n_G must be very small because of the bandgap, so the in-plane resistance can be large and ΔV can be substantial. As long as n_G is negligible the bands will not be renormalized and ΔV can be identified with the purely electrostatic energy shift of an ARPES spectral feature. $\Delta E_\Gamma/e$ in Fig. 3 indeed tracks V_G closely at low V_G values (see Extended Data Fig. 7). We deduce that, in this regime, photoemission directly from the BN valence band generates conductivity in the BN that is sufficient to keep the potential in the MX_2 close to that of the gate, that is, ΔV is approximately equal to V_g, with negligible potential drop across the BN and no accumulation of charge in the MX_2. By contrast, at a sufficiently large magnitude of V_G, $(V_G - \Delta E_\Gamma/e)$ tends towards a linear increase with V_G. This happens when the high doping makes the in-plane resistance R small enough that the electrochemical potential in the MX_2 approaches that in the (ground) electrode and ΔV stops changing, with the Fermi energy virtually pinned at the band edge owing to the large density of states. In this regime we can take $n_G = C_g(V_G - \Delta E_\Gamma/e)$, since $(V_G - \Delta E_\Gamma/e)$ is the static potential drop across the BN, the electrons are in electrochemical equilibrium, and the quantum capacitance is negligible (that is, E_F is effectively pinned at the CBE). The values of n_G shown in Fig. 4 are obtained in this way.

Our interpretation of the behaviour in Fig. 3 for monolayer WSe_2 is as follows. The photoemission current I_{PE}, the current to the contact I_C, and the current to the gate I_G (indicated in the sketch at the top left of Fig. 3) must sum to zero. I_G can be substantial because of photoexcited carriers in the BN. (It should be borne in mind that in general such currents may cause a device to operate differently from how it would in the dark.) Between B and C in Fig. 3, the WSe_2 is depleted and insulating enough that the BN photoconductivity brings the potential close to that of the gate. Holes created by photoemission from the WSe_2 recombine with excited electrons in the BN, and I_{PE} is approx. equal to I_G. Between C and D, these holes can also drift to the contact through the depleted WSe_2, and I_C is substantial. Above threshold, at E, electrons accumulate at the CBE in the WSe_2 as they flow in laterally from the graphene contact, and the CBE is pinned close to the graphene Fermi level. Similarly, at A, holes accumulate and the valence-band edge is pinned. An 'overshoot' occurs at D because when the CBE in the beam spot first moves below the graphene Fermi level, the Schottky barrier between graphene and WSe_2 prevents electrons flowing in fast enough to accumulate.

Estimating the CBE energy. The structure of the conduction band is not resolvable in the ARPES data (Fig. 2d–f). The density of states at a single parabolic band edge is $g_{2D} = g_sg_vm^*/\hbar^2$, with spin and valley degeneracies g_s and g_v and effective mass m^*. For 1L WSe_2 the conduction-band edges are at the K-points, so $g_v = 2$, and the band is spin-split by approximately 40 meV (ref. [40]); hence $g_s = 1$ for moderate doping. Calculations[40] show that m^* is approximately equal to $0.3m_e$. Using $n_G = \int_{E_c}^{\infty} F(E)g_{2D}dE$, where $F(E)$ is the Fermi–Dirac distribution, then gives that $E_F - E_C$ is approximately equal to 30 meV at $n_G = 1.0 \times 10^{13}$ cm^{-2}.

Optical spectroscopy. Photoluminescence measurements were performed using approximately 20-μW linearly polarized 532-nm continuous-wave laser excitation in reflection geometry, with the signal collected by a spectrometer and a silicon charge-coupled device, in vacuum in a closed-cycle cryostat.

Electronic-structure calculations including spin–orbit interaction were made using the Quantum Espresso DFT package[41]. Structures were first optimized until forces were smaller than 10^{-4} Ry $Bohr^{-1}$. Geometry optimizations and band-structure calculations were performed with an 18 × 18 in-plane k-point grid with a plane-wave energy cut-off of 140 Ry. To avoid interaction between periodic images, the vacuum spacing was 25.0 Å. We used norm-conserving fully relativistic pseudopotentials[42] from PseudoDojo[43], where the semi-core 4d, 5s and 5p states for tungsten are retained as valence electrons. This results in a lattice constant of 3.32 Å for all three structures. We used the results from calculations with the PBE functional as a starting point for G_0W_0 calculations which used the Yambo code[44], with the Godby–Needs plasmon pole approximation[45]. We used 300 bands, 500 bands and 700 bands for the monolayer, bilayer and trilayer WSe_2, respectively, for the self-energy and dynamical dielectric screening. In order to treat the divergence of the Coulomb interaction during the self-energy calculation, we used the random integration method[46], with 3×10^6 random q-points and 100 random $\boldsymbol{G}$ vectors.

Data availability

All data presented in this paper are available at http://wrap.warwick.ac.uk/116301. Additional data related to this paper may be requested from the authors.

34. Zomer, P. J., Guimarães, M. H. D., Brant, J. C., Tombros, N. & Van Wees, B. J. Fast pick up technique for high quality heterostructures of bilayer graphene and hexagonal boron nitride. *Appl. Phys. Lett.* **105**, 013101 (2014).
35. Fang, T., Konar, A., Xing, H. & Jena, D. Carrier statistics and quantum capacitance of graphene sheets and ribbons. *Appl. Phys. Lett.* **91**, 092109 (2007).

36. Yu, G. L. et al. Interaction phenomena in graphene seen through quantum capacitance. *Proc. Natl Acad. Sci. USA* **110**, 3282–3286 (2013).
37. Dean, C. R. et al. Boron nitride substrates for high-quality graphene electronics. *Nat. Nanotechnol.* **5**, 722–726 (2010).
38. Kim, K. K. et al. Synthesis and characterization of hexagonal boron nitride film as a dielectric layer for graphene devices. *ACS Nano* **6**, 8583–8590 (2012).
39. Mucha-Kruczyński, M. et al. Characterization of graphene through anisotropy of constant-energy maps in angle-resolved photoemission. *Phys. Rev. B* **77**, 195403 (2008).
40. Kormányos, A. et al. k·p theory for two-dimensional transition metal dichalcogenide semiconductors. *2D Mater.* **2**, 022001 (2015).
41. Giannozzi, P. et al. QUANTUM ESPRESSO: a modular and open-source software project for quantum simulations of materials. *J. Phys. Condens. Matter* **21**, 395502 (2009).
42. Hamann, D. R. Optimized norm-conserving Vanderbilt pseudopotentials. *Phys. Rev. B* **88**, 085117 (2013).
43. van Setten, M. J. et al. The PSEUDODOJO: training and grading a 85 element optimized norm-conserving pseudopotential table. *Comput. Phys. Commun.* **226**, 39–54 (2018).
44. Marini, A., Hogan, C., Grüning, M. & Varsano, D. yambo: an ab initio tool for excited state calculations. *Comput. Phys. Commun.* **180**, 1392–1403 (2009).
45. Godby, R. W. & Needs, R. J. Metal-insulator transition in Kohn-Sham theory and quasiparticle theory. *Phys. Rev. Lett.* **62**, 1169–1172 (1989).
46. Castro, A., Räsänen, E. & Rozzi, C. A. Exact Coulomb cutoff technique for supercell calculations in two dimensions. *Phys. Rev. B* **80**, 033102 (2009).

Acknowledgements Our research into monitoring gated electronic structure changes is supported as part of Programmable Quantum Materials, an Energy Frontier Research Center funded by the US Department of Energy (DOE), Office of Science, Basic Energy Sciences (BES), under award DE-SC0019443. Initial development of the samples and technique was done under award DE-SC0002197 via D.H.C. and P.V.N. Optical spectroscopy and partial sample fabrication were supported by award DE-SC0018171 (via X. Xu and N.P.W.). P.V.N. and J.K. received partial support from NSF Materials Research Science and Engineering Centers (MRSEC) award 1719797. N.R.W. and N.D.M.H. were supported through UK Engineering and Physical Sciences Research Council (EPSRC) award EP/P01139X/1. N.C.T., N.Y. and A.J.G. were supported through EPSRC studentships (EP/M508184/1 and EP/R513374/1). X. Xia was supported by a University of Warwick studentship. N.D.M.H. and G.C.C. were supported by the Winton Programme for the Physics of Sustainability. G.C.C. was supported by the Cambridge Trust European Scholarship. Computing resources were provided by the Darwin Supercomputer of the University of Cambridge High Performance Computing Service, the Scientific Computing Research Technology Platform of the University of Warwick, and the UK national high-performance computing service, ARCHER, via the UKCP consortium (EP/P022561/1).

Author contributions N.R.W., X. Xu and D.H.C. conceived and supervised the project. P.V.N., J.K. and N.P.W. fabricated the samples. N.C.T., N.R.W., P.V.N., X. Xia, A.J.G., V.K., A.G. and A.B. collected μ-ARPES data. N.C.T., N.R.W. and P.V.N. analysed μ-ARPES data (with input from A.B.). N.P.W. acquired photoluminescence data. N.D.M.H., N.Y. and G.C.C. performed the band-structure calculations. D.H.C., N.R.W., P.V.N. and X. Xu wrote the paper with input from all authors.

Competing interests The authors declare no competing interests.

Additional information

Correspondence and requests for materials should be addressed to D.H.C., X.Xu or N.R.W.

Peer review information *Nature* thanks Adam Shaffique, Shuyun Zhou and the other anonymous reviewer(s) for their contribution to the peer review of this work.

Reprints and permissions information is available at http://www.nature.com/reprints.

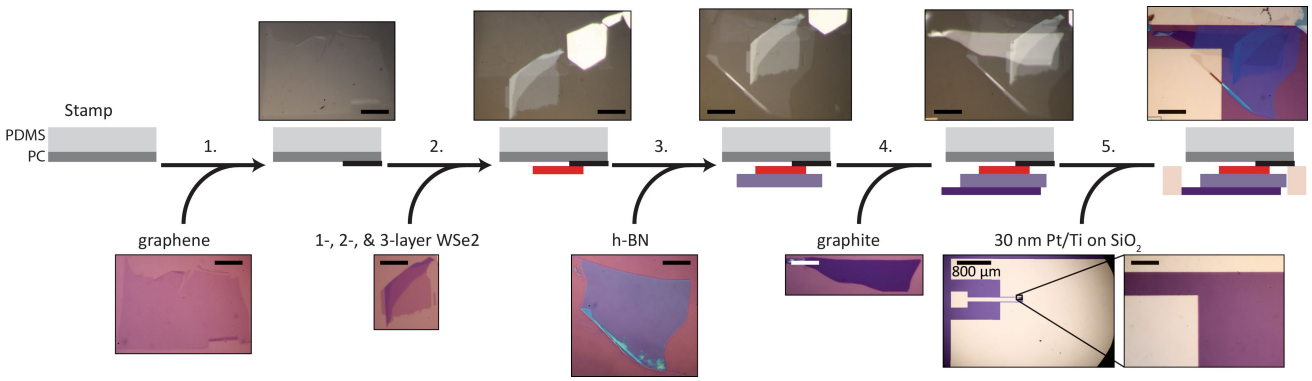

Extended Data Fig. 1 | Fabrication of a gated heterostructure. Diagram showing the process for fabricating WSe_2 device 1, with associated micrographs. Scale bars are 15 µm unless otherwise noted. PC, polycarbonate; PDMS, polydimethylsiloxane.

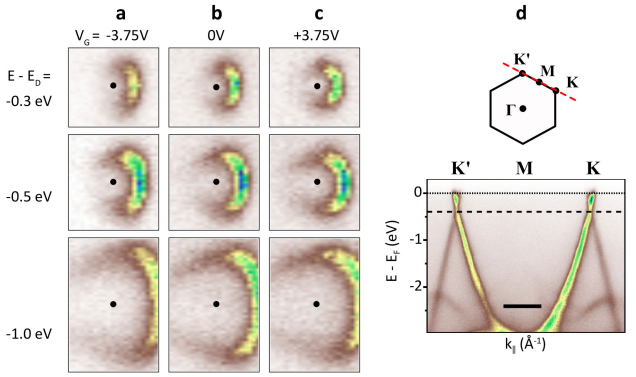

Extended Data Fig. 2 | Distortion-free, uniform band shifting in electrostatically gated graphene. a–c, Constant energy slices through a graphene Dirac cone at the stated gated voltages and electron energies relative to the Dirac point (black dot). No substantial change is seen on varying V_G, implying that the spectrum is not distorted by electrostatic/space charge effects. The width of each panel represents 4 $Å^{-1}$. **d**, Bottom, slice of energy E versus in-plane momentum $k_{||}$ along the zone boundary, through points K and K′ (shown at the top), in gated graphene at $V_G = +3.35$ V. Scale bar, 0.5 $Å^{-1}$. The spectrum is symmetric about point M, as illustrated by the consistent Dirac-point energy (dashed line) between K and K′. These measurements are from the same device as Fig. 3, from a region in which the graphene was on top of the 1L WSe_2 (which produces the faint bands at binding energies of around 2 eV) but still electrostatically gated. This shows that the electric field from the gate does not distort the measured graphene spectrum in any direction in momentum space.

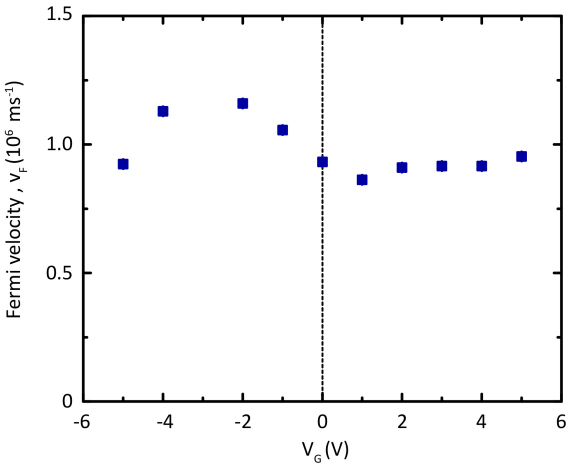

Extended Data Fig. 3 | Extracted graphene Fermi velocity versus gate voltage. We calculated the Dirac-point energy and Fermi velocity from $E - k$ slices (some of which are shown in Fig. 1) near the graphene K point, by analysing the band dispersions. We extracted momentum-distribution curves (MDCs; that is, intensity as a function of momentum $I(k)$ at constant energy), and found the positions of the branches on each side of the Dirac cone by fitting Gaussian peaks. After repeating this process for each MDC within $|E - E_F| < 1$ eV, we fit a straight line of the same absolute slope to each side, yielding the Dirac point, E_D, from where the lines cross and the Fermi velocity, v_F, from their slope. In cases in which one side was much more intense than the other, we used only the more intense side to find v_F. The extracted velocity is here plotted against gate voltage. Evidence has previously been reported[36] of a reduction in v_F of up to 20% near E_D in graphene films at low doping levels (roughly 1×10^{12} cm^{-2}). This corresponds to a subtle distortion of the bands at E_D, which the spectrometer at Elettra does not as yet have the resolution to probe, and could not be detected by the above procedure which assumes purely linear dispersion. Note that the variations seen in this figure can be explained by systematic errors, taking into account experimental limitations such as the very weak emission from one branch and the sensitivity to the exact alignment of the momentum slice with the Dirac point.

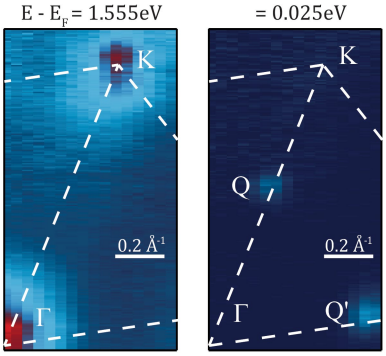

Extended Data Fig. 4 | Uniform band shifting in electrostatically gated 2L WSe_2. Constant energy maps of electrostatically gated 2L WSe_2 at $V_G = +8$ V: left, at a binding energy of 1.555 eV, which here corresponds to the valence-band maximum; and right, near the Fermi energy at a binding energy of 0.025 eV. It can be seen that the CBE is the same at points Q and Q′, implying that the gate field does not substantially distort the spectrum in this case either.

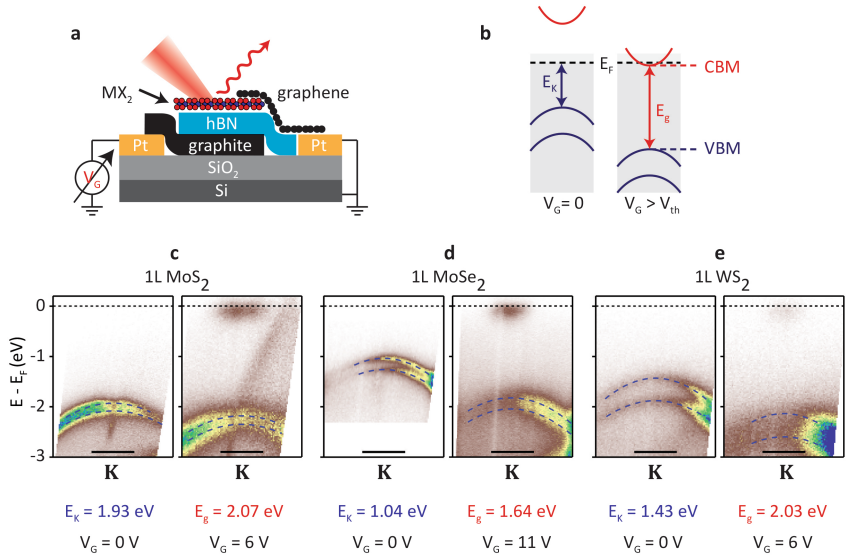

Extended Data Fig. 5 | CBEs in monolayer MoS_2, $MoSe_2$ and WS_2. **a**, Diagram of a device, with graphene contact grounded and gate voltage applied to the graphite back gate, as in Fig. 2a. **b**, Diagram showing the bands near point K, at zero gate voltage (left) and at a gate voltage that exceeds the threshold voltage to bring the Fermi level to the CBE (right). CBM, conduction-band maximum; VBM, valence-band maximum. **c**–**e**, Energy-momentum slices through point for monolayer MoS_2, $MoSe_2$ and WS_2. Scale bars, 0.3 $Å^{-1}$.

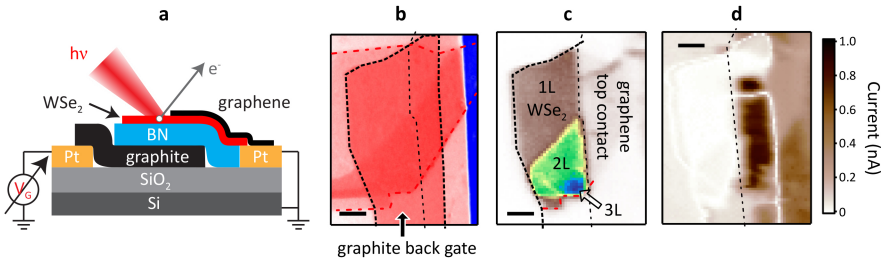

Extended Data Fig. 6 | Photocurrent and SPEM maps of a WSe_2 heterostructure device. a, Diagram of the device, with the graphene contact grounded and a gate voltage applied to the graphite back gate. **b**, **c**, Optical (**b**) and SPEM (**c**) images of WSe_2 device 1, with 1L, 2L and 3L regions identified. Dashed lines trace boundaries of the graphite gate (red) and the graphene contact (black). **d**, Photocurrent image acquired simultaneously with the SPEM image in panel **c**. Scale bars, 5 μm.

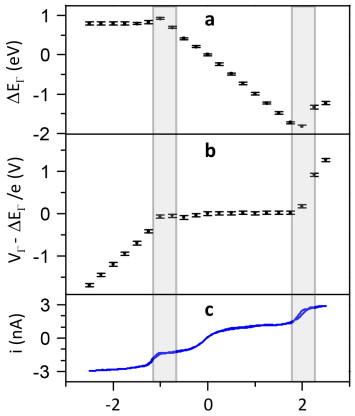

Extended Data Fig. 7 | Gate-induced band shifts and photocurrent in monolayer WSe_2. a, ΔE_Γ versus V_G for WSe_2 monolayer device 2. **b**, $V_G - \Delta E_\Gamma/e$ versus V_G. **c**, Current from gate to ground versus V_G. The grey shaded regions indicate the threshold regions in which the WSe_2 becomes conducting. See Methods for discussion.